nature nanotechnology

ARTICLES

PUBLISHED ONLINE: 8 JUNE 2015 | DOI: 10.1038/NNANO.2015.115

Syringe-injectable electronics

Jia Liu[1†], Tian-Ming Fu[1†], Zengguang Cheng[1,2†], Guosong Hong[1], Tao Zhou[1], Lihua Jin[3], Madhavi Duvvuri[1], Zhe Jiang[1], Peter Kruskal[1], Chong Xie[1], Zhigang Suo[3], Ying Fang[2*] and Charles M. Lieber[1,3*]

Seamless and minimally invasive three-dimensional interpenetration of electronics within artificial or natural structures could allow for continuous monitoring and manipulation of their properties. Flexible electronics provide a means for conforming electronics to non-planar surfaces, yet targeted delivery of flexible electronics to internal regions remains difficult. Here, we overcome this challenge by demonstrating the syringe injection (and subsequent unfolding) of sub-micrometre-thick, centimetre-scale macroporous mesh electronics through needles with a diameter as small as 100 μm. Our results show that electronic components can be injected into man-made and biological cavities, as well as dense gels and tissue, with >90% device yield. We demonstrate several applications of syringe-injectable electronics as a general approach for interpenetrating flexible electronics with three-dimensional structures, including (1) monitoring internal mechanical strains in polymer cavities, (2) tight integration and low chronic immunoreactivity with several distinct regions of the brain, and (3) *in vivo* multiplexed neural recording. Moreover, syringe injection enables the delivery of flexible electronics through a rigid shell, the delivery of large-volume flexible electronics that can fill internal cavities, and co-injection of electronics with other materials into host structures, opening up unique applications for flexible electronics.

The emergence of flexible electronics has significantly extended the applications of electronics by allowing intimate interfaces between electronic units and non-planar surfaces for better monitoring and manipulation of their properties[1–3]. A variety of electronic devices[1–8] have been integrated on flexible and stretchable substrates, enabling applications from foldable displays to electronic skin[3–8]. Three-dimensional (3D) interpenetration of flexible electronics within existing structures could further broaden and open up new applications by directly interfacing devices with the internal structures of man-made and biological materials.

Recent work has shown that flexible electronics can be placed into 3D structures through surgical processes[9–12] or by being attached to and subsequently released from a rigid delivery substrates[13,14] for biological and biomedical applications. However, direct 3D interpenetration of electronics within these structures is limited by the intrinsic thin-film[14] supporting substrates. We have previously introduced a macroporous mesh paradigm that allows electronics to be combined with polymer precursors and cells to yield 3D interpenetration[15,16], although controlled delivery and/or non-surgical placement of these ultraflexible open electronic networks into structures with seamless 3D integration and interpenetration has not been possible.

Here, we describe the design and demonstration of macroporous flexible mesh electronics, where the electronics can be precisely delivered into 3D structures by syringe injection, whereupon they subsequently relax and interpenetrate within the internal space of man-made and biological materials. Distinct from previous reports[3,17,18], syringe injection requires the complete release of the mesh electronics from a substrate so that the electronics can be driven by solution through a needle. The syringe-injectable electronics concept involves (1) loading the mesh electronics into a syringe and needle, (2) insertion of the needle into the material or internal cavity and initiation of mesh injection (Fig. 1a), (3) simultaneous mesh injection and needle withdrawal to place the electronics into the targeted region (Fig. 1b), and (4) delivery of the input/output (I/O) region of the mesh outside the material (Fig. 1c) for subsequent bonding and measurements.

Implementation of electronics for syringe injection

The mechanical properties of the free-standing mesh electronics are important to the injection process. The basic mesh structure (Fig. 1d and Supplementary Fig. 1a,b) consists of longitudinal polymer/metal/polymer elements, which function as interconnects between exposed electronic devices and I/O pads and transverse polymer elements. The mesh longitudinal and transverse bending stiffness, D_L and D_T, are determined by the mesh unit cell, the corresponding widths and thicknesses of the longitudinal and transverse elements, and the angle α (refs 15, 16). Simulations of D_T and D_L versus α (Fig. 1e) show that D_T (D_L) decreases (increases) with increasing α. Hence, increasing α facilitates bending along the transverse direction (reduced D_T) and should allow for rolling-up of the mesh electronics within a needle constriction, while at the same time increasing D_L, which should reduce bending and potential buckling along the injection direction.

The mesh electronics were fabricated, fully released from the substrates using reported methods[15,16], and loaded into glass needles connected to a microinjector (Supplementary Sections 2 and 3 and Supplementary Figs 2 and 3). The image in Fig. 1f of the injection of a 2-mm-wide sample through a glass needle with an inner diameter (ID) of 95 μm shows the compressed mesh ~250 μm from the needle opening, which is then injected ~0.5 cm into ×1 phosphate-buffered saline (PBS) solution. The 3D image in Fig. 1g highlights the unfolding of this mesh structure from the point of the needle constriction (blue dashed box). Higher-resolution images (Supplementary Fig. 4a,b) show that the mesh structure is continuous as it unfolds. Similar results were obtained for the injection of a sample (width of 1.5 cm) through a 20 gauge (600 μm ID) metal needle (Supplementary Fig. 4c), demonstrating

[1]Department of Chemistry and Chemical Biology, Harvard University, Cambridge, Massachusetts 02138, USA. [2]National Center for Nanoscience and Technology, 11 Beiyitiao Street, Zhongguancun, Beijing 100190, China. [3]School of Engineering and Applied Sciences, Harvard University, Cambridge, Massachusetts 02138, USA. †These authors contributed equally to this work. *e-mail: fangy@nanoctr.cn; cml@cmliris.harvard.edu

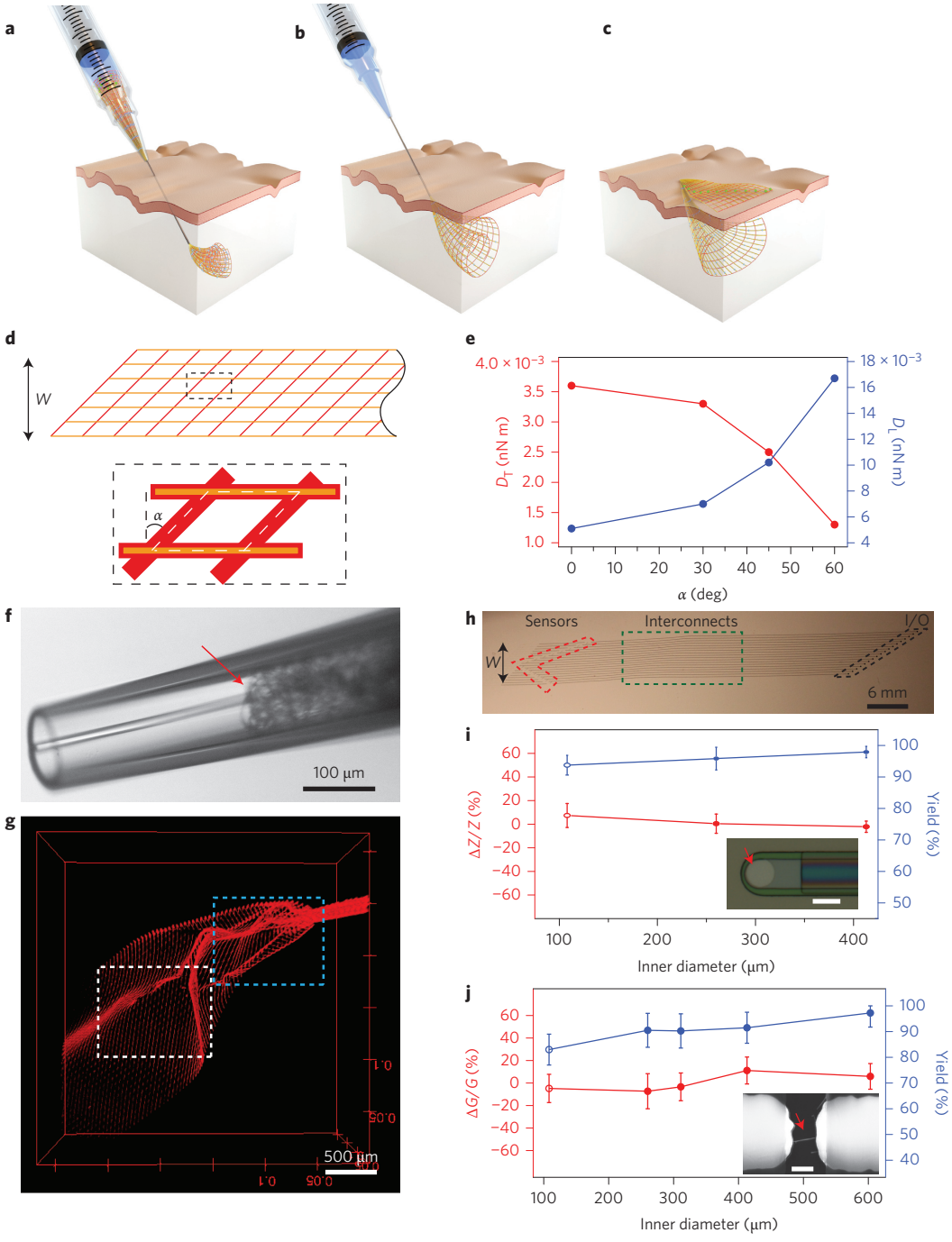

Figure 1 | Syringe-injectable electronics. a–c, Schematics of injectable electronics. Red-orange lines highlight the overall mesh structure and indicate the regions of supporting and passivating polymer mesh layers. Yellow lines indicate metal interconnects between I/O pads (green filled circles) and recording devices (blue filled circles). **d**, Schematic of the mesh electronics design (top). Orange and red lines represent polymer-encapsulated metal interconnects and supporting polymer elements, respectively, and W is the total width of the mesh. The dashed black box (bottom) highlights the structure of one unit cell (white dashed lines), where α is the angle of deviation from rectangular. **e**, Longitudinal mesh bending stiffness D_L and transverse mesh bending stiffness D_T as a function of α (defined in **d**). **f**,**g**, Images of mesh electronics injection through a glass needle (ID = 95 μm) into ×1 PBS solution: bright-field microscopy image of the mesh electronics immediately before injection into solution (**f**, the red arrow indicates the end of the mesh inside the glass needle); 3D reconstructed confocal fluorescence image recorded following injection of ~0.5 cm mesh electronics into ×1 PBS solution (**g**). Blue and white dashed boxes in **g** correspond to the regions shown in Supplementary Fig. 3a,b. **h**, Optical image of an injectable mesh electronics structure unfolded on a glass substrate (W is the total width of the mesh electronics). The red dashed polygon highlights the position of electrochemical devices or FET devices. Green and black dashed boxes highlight metal interconnect lines and metal I/O pads, respectively. **i**,**j**, Yields and change (with ±1 standard deviation, s.d.) in properties post-injection for single-terminal electrochemical and two-terminal FET devices. In **i**, yield (blue) and impedance change (red) are shown for metal electrodes from mesh electronics injected through 32, 26 and 22 gauge metal needles. Inset: bright-field image of a representative metal electrode on the mesh electronics, where the sensing electrode is highlighted by a red arrow. Scale bar, 20 μm. In **j**, yield (blue) and conductance change (red) are shown for silicon nanowire FETs following injection through 32, 26, 24, 22 and 20 gauge needles. Inset: scanning electron microscopy (SEM) image of a representative nanowire FET device in the mesh electronics. The nanowire is highlighted by a red arrow. Scale bar, 2 μm.

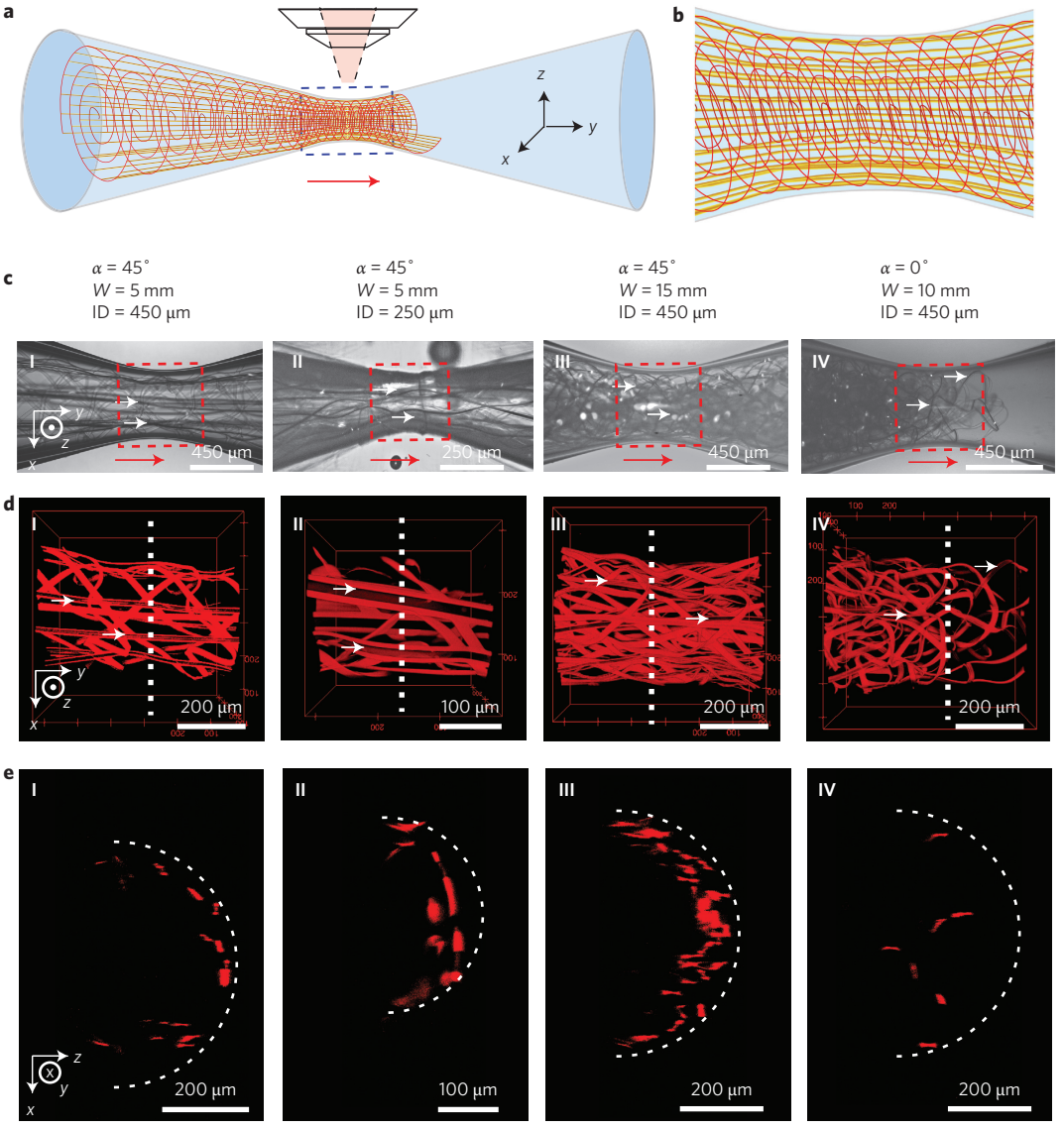

Figure 2 | Imaging of the mesh electronics structure in needle constrictions. a, Schematic illustrating the structure of a pulled glass tube (blue) with mesh electronics passing from the larger (left) to smallest (centre) ID of the tube. The red arrow indicates the direction of injection, and the *x*, *y* and *z* axes indicate coordinates relative to the microscope objective for images in **c**–**e**. **b**, Schematic image of the mesh structure from the region of the constriction indicated by the blue dashed box in **a**. **c**, Bright-field microscopy images of different design mesh electronics injected through glass channels. I and II ($W = 5$ mm, $\alpha = 45°$): mesh electronics injected through glass channels with 450 and 250 μm ID, respectively. III ($W = 15$ mm, $\alpha = 45°$): mesh electronics injected through a 450 μm ID glass channel. IV ($W = 10$ mm, $\alpha = 0°$): mesh electronics injected through a 450 μm ID glass channel. The injection direction is indicated by red arrows. The orientation relative to the axes in **a** is indicated in I and is the same for II to IV. **d**, 3D reconstructed confocal images from the dashed red box regions in **c**, I–IV. The *x*, *y* and *z* axes in I are the same for II to IV. Small white horizontal arrows in **c** and **d** indicate several of the longitudinal elements containing metal interconnects in the mesh electronics. **e**, Cross-sectional images plotted as half cylinders from positions indicated by the vertical white dashed lines in **d**. White dashed curves indicate the approximate IDs of the glass constrictions.

the generality of this injection through common glass and metal syringe needles.

To test further the electrical continuity and functionality of the mesh electronics post-injection, we used anisotropic conductive film (ACF)[19] to connect the I/O pads of the electronics post-injection to flexible cables that were interfaced to measurement electronics (Supplementary Fig. 5a–d). Studies of the electrical performance and yield of the devices following injection into ×1 PBS solution through 100–600 μm ID needles (Fig. 1i,j) highlighted several points. First, the metal electrochemical devices had an average device yield >94% and an average device impedance change (an important characteristic for voltage sensing applications[20,21]) of <7% post-injection (Fig. 1i). Second, the silicon nanowire field-effect transistor (FET) devices had a yield >90% for needle IDs from 260 to 600 μm, only dropping to 83% for the smallest 100 μm ID needles, and exhibited <12% conductance change on average post-injection (Fig. 1j). Together, these results demonstrate the robustness of our mesh electronics design and the capability of maintaining good device performance following injection through a wide range of needle IDs.

We characterized the structures of different mesh electronics within glass needle-like constrictions to understand the design parameters for successful injection (Fig. 2a,b). Bright-field microscopy images of mesh electronics with different structural parameters recorded from the central region of glass channels with different IDs (Fig. 2c) highlight two important features. First, mesh

electronics with $\alpha = 45°$ and widths substantially larger than the constriction ID can be smoothly injected. Relatively straight longitudinal elements are seen in Fig. 2c,I and II, where the 5 mm two-dimensional mesh widths are 11 and 20 times larger than the respective 450 and 250 μm ID needle constrictions. Second, even mesh electronics with a width of 1.5 cm (Fig. 2c,III) can be injected smoothly through a 33 times smaller ID (450 μm) constriction.

The corresponding 3D reconstructed confocal images with higher resolution of $\alpha = 45°$ mesh electronics samples with mesh width/constriction ID ratios from 11 to 33 (Fig. 2d,I to III) highlight several important points. First, the longitudinal elements maintain a straight geometry without substantial bending through the constriction, even for the 33:1 ratio (Fig. 2d,III). Second, these images show that the transverse elements bend with a curvature that matches the needle ID, and the longitudinal elements and estimated number of rolls of the mesh at the needle constriction are comparable to geometric calculations (Supplementary Section 5.1). This latter point and further structural details can be seen in cross-sectional plots of these 3D images (Fig. 2e,I–III), which highlight uniformly organized transverse and longitudinal elements near the IDs of the glass constriction. Third, there is no evidence for fracture of the $\alpha = 45°$ design mesh elements. Indeed, simulations of the strain versus needle ID show that the upper limit strain value for the mesh in a 100-μm-ID needle, ~1%, is less than the calculated critical fracture strain (Supplementary Section 5.2.3).

In contrast, bright-field and 3D confocal images recorded from the injection of $\alpha = 0°$ mesh electronics (Fig. 2c–e,IV) and thin-film electronics (Supplementary Fig. 6) show that these structures are not smoothly injected through the needle-like constrictions. Specifically, images of a mesh sample with $\alpha = 0°$ (Fig. 2d,IV) but a smaller width than $\alpha = 45°$ (Fig. 2d,III) exhibit jammed mesh at the constriction. The structure is deformed and fills the cross-section of the channel (Fig. 2e,IV), rather than rolling up as observed for $\alpha = 45°$. Injection of thin-film electronics with the same thickness and total width as the mesh in Fig. 2c,I for a width/needle ID ratio of 11 became jammed in the channel (Supplementary Fig. 6a,I). Reducing the thin-film width/needle ID ratio to 4 did lead to successful injection (Supplementary Fig. 6a,II), although 3D confocal microscopy images (Supplementary Fig. 6b,c) show substantial buckling of the structure, in contrast to our $\alpha = 45°$ mesh design. These results confirm that the reduced transverse bending stiffness for the $\alpha = 45°$ design plays a key role in allowing the mesh electronics to smoothly roll up, follow the needle ID with minimum strain, and thereby allow for the injection of two-dimensional widths >30 times the needle ID.

Injection of electronics into synthetic structures

We have investigated several applications of our syringe-injectable electronics, including the delivery of electronics to internal regions of man-made structures and live animals. First, mesh electronics incorporating addressable silicon nanowire piezoresistive strain sensors[16] were co-injected with polymer precursors through a small injection site (Fig. 3a, Supplementary Fig. 8a and Supplementary Section 3.5.1) into polydimethylsiloxane (PDMS) cavities, with I/O pads ejected outside the structure. Visual inspection, micro-computed tomography (μCT) images and photographs (Fig. 3b and Supplementary Fig. 8b) demonstrate that the mesh electronics unfolds and smoothly follows the internal cavity structure with continuous metal interconnects.

We monitored the response of the internal nanowire piezoresistive strain sensors as the PDMS structures were deformed. Plots of strain recorded simultaneously for four typical calibrated devices (d1–d4, Fig. 3c) versus deformation with a point load along the

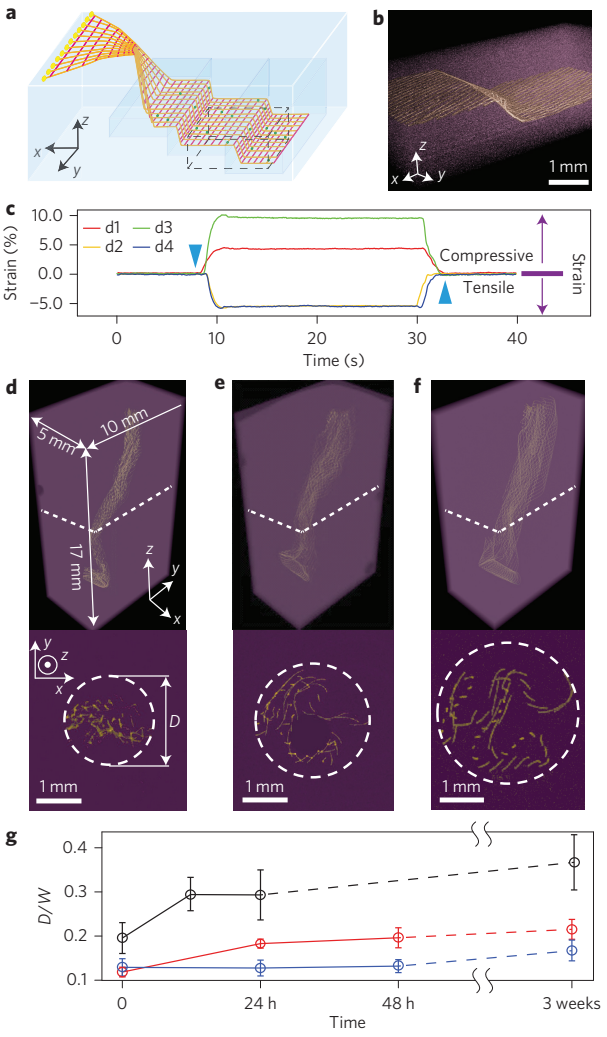

Figure 3 | Syringe injection of mesh electronics into 3D synthetic structures. **a**, Schematic of mesh electronics injected with an uncured PDMS precursor into a PDMS cavity (blue) with I/O pads unfolded outside the cavity. The injected PDMS precursors were cured after injection. Red lines highlight the overall mesh structure and indicate the regions of supporting and passivating polymers, and yellow lines indicate the metal interconnects between I/O pads (yellow filled circle) and devices (dark green filled circle). **b**, μCT image showing the zoomed-in structure highlighted by the black dashed box in **a** and Supplementary Fig. 7b. False colours were applied for the metal lines (yellow) in PDMS (purple). **c**, Four-nanowire device response to pressure applied on the PDMS. Blue downward and upward pointing triangles denote the time points when the strain was applied and released, respectively. Purple downward and upward arrows show the tensile and compressive strains, corresponding to the minus and plus change in conductance, respectively. **d**–**f**, Upper images: 3D reconstructed μCT images of mesh electronics injected into 75% Matrigel after incubation for 0 h (**d**), 24 h (**e**) and 3 weeks (**f**) at 37 °C. The *x*, *y* and *z* axes are shown in **d** and apply to **e** and **f**, where the injection direction is approximately along the *z* axis. In **d**–**f**, false colours were applied with metal lines in the mesh in yellow and the Matrigel in purple. Lower images: corresponding cross-section images at $z = 10$ mm with thickness of 500 μm. The positions of the cross-sections are indicated by white dashed lines in the upper images. The maximum extent of unfolding of the mesh electronics is highlighted by white dashed circles (with diameter *D*) in each image. **g**, Time dependence of mesh electronics unfolding following injection into 25% (black), 75% (red) and 100% (blue) Matrigel. Measured diameter *D* was normalized by the 2D width *W* of the fabricated mesh electronics. *D* was sampled from five cross-sections taken at $z = 5$, 7.5, 10, 12.5 and 15 mm to obtain the average ± 1 s.d.

z axis show compressive (d1, d3) and tensile (d2, d4) local strains recorded by the nanodevices. Mapping the strain response onto the optical image of the electronics/PDMS hybrid shows the nanowire sensors separated by up to 4 mm (Supplementary Fig. 8c), with the compressive and tensile strains consistent with expectation for the point-like deformation. These data suggest that syringe injection of mesh electronics with piezoresistive devices could be used to monitor and map internal strains within structural components with gaps/cracks in a manner that is not currently possible, and more generally, to simultaneously monitor corrosion and strain within internal cavities or cracks by using nanowire devices to also measure pH and other chemical changes[22].

Second, we investigated 3D gel structures without cavities as representative models of mesh electronics injection into soft materials and biological tissue. Images recorded versus time following the injection of mesh electronics into Matrigel, a scaffold used in neural tissue engineering (Fig. 3d–f)[23], show that the mesh unfolds ~80% in the radial direction over a three-week period at 37 °C. As expected, the degree of unfolding of the mesh electronics within the Matrigel depends on the gel concentration for fixed mesh mechanical properties (Fig. 3g), with ~90 and 30% unfolding for 25 and 100% Matrigel, respectively. The ability to inject and observe partial unfolding of the electronics within gels with tissue-like properties also suggests that co-injection with other biomaterials[24] and/or cells[25] could be another application of injectable mesh electronics. Indeed, preliminary experiments show that co-injection of mesh electronics and embryonic rat hippocampal neurons into Matrigel leads to 3D neural networks with neurites interpenetrating the mesh electronics (Supplementary Fig. 8d,e). These co-injection results highlight potential opportunities for tissue engineering and stem cell therapy[25].

Injection of mesh electronics into live rodent brains

Finally, we investigated the behaviour of mesh electronics stereotaxically injected into the lateral ventricle (LV) and hippocampus (HIP) of live rodents (Fig. 4a–d and Supplementary Section 3.6)[26], where the capability to deliver electronics (with widths on the scale of millimetres) through needles with outer diameters (ODs) on the scale of hundreds of micrometres allows for a much smaller window in the skull than the usual widths of electronics, thereby reducing the invasiveness of the surgery. Confocal microscopy images recorded from tissue slices from the LV region prepared five weeks post-injection of the mesh electronics (Fig. 4e–g and Supplementary Fig. 9) demonstrate several important points. First, the mesh electronics relaxes from the initial ~200 μm injection diameter to bridge the caudoputamen (CPu) and lateral septal nucleus (LSD) regions, which define the boundaries of the cavity in this slice (Fig. 4e). Second, higher-resolution images from the boundary between the electronics and the CPu/subventricular zone (Fig. 4f and Supplementary Fig. 9a) show that the mesh electronics interpenetrates with the boundary cells and that cells stained with neuron marker NeuN associate tightly with the mesh. Third, control images recorded from the same tissue slice but the opposite hemisphere (without injected mesh electronics; Supplementary Fig. 9b,d–f) show that the level of glial fibrillary acidic protein (GFAP) expression is similar with and without the injected mesh electronics, indicating little chronic tissue response to the mesh electronics. Fourth, images of the mesh electronics in the middle of the LV (Fig. 4g and Supplementary Fig. 9c) show a large number of 4′,6-diamidino-2-phenylindole (DAPI) stained cells bound to the mesh structure. These images indicate that (1) the mesh expands to integrate within the local extracellular matrix (that is, the mesh is neurophilic), (2) cells form tight junctions with the mesh, and (3) neural cells migrate hundreds of micrometres from the subventricular zone along the mesh structure[27]. Notably, these results suggest using injectable electronics to mobilize and monitor neural cells from the LV region following brain injury[28] as well as delivering mesh electronics to other biological cavities for recording and stimulation.

We also injected mesh electronics into the dense tissue of the HIP (Fig. 4d). Bright-field images of coronal tissue slices, prepared five weeks post-injection (Fig. 4h and Supplementary Fig. 10a,b), demonstrate that the electronics is fully extended in the longitudinal direction. The mesh only relaxes a small amount with respect to the initial injection diameter (red dashed lines in Fig. 4h), because the force required to bend the mesh[16] is comparable to the force needed to deform the tissue[23,29]. In addition, an overlay of bright-field and DAPI epi-fluorescence images (Fig. 4i) shows that the injection did not disrupt the CA1 and dentate gyrus (DG) layers of this region. The confocal images (Fig. 4j and Supplementary Figs 10c, 11 and 12) highlight the unique characteristics of the injectable mesh electronics in dense neural tissue. First, analysis of GFAP fluorescence shows that there is limited or no astrocyte proliferation near the mesh, although the full image (Fig. 4j) indicates a reduction in cell density at the central region of injection. Significantly, analysis of similar horizontal slice samples prepared from three independent mesh injections (Supplementary Figs 11 and 12a,b) also show limited or no astrocyte proliferation around our electronics, and quantitative analyses (Supplementary Figs 11b,II and 12b) demonstrate that GFAP values versus distance from and along the mesh electronics surface are similar to the background level. Second, these images show healthy neurons (NeuN signal) surrounding and close to the SU-8 ribbons of the mesh (Fig. 4j and Supplementary Figs 10c and 12c). Data and analyses from three independent samples (Supplementary Figs 11 and 12d,I) quantitatively support this observation. Specifically, quantitative analyses (Supplementary Figs 11b,I and 12d) demonstrate that the NeuN signals versus distance from and along the mesh electronics surface are enhanced or similar to background levels. These observations, which are similar to our results for injections into the LV, show the capability of the mesh electronics to promote positive cellular interactions, in contrast to the reported chronic responses of neural tissue following the insertion of silicon[30], metal[13], polyimide[31]/SU-8[32] or ultrasmall carbon[33] electrical probes, which reduced the neuron density and enhanced the astrocyte density near the probes/tissue interface.

We attribute the unique biocompatibility of our syringe-injected mesh electronics to their ultra-small bending stiffness and micrometre-scale features. The bending stiffness of the injected mesh electronics (0.087 nN m) is four to six orders of magnitude smaller than the values reported for previous implantable electronics, such as silicon (4.6×10^5 nN m)[30,34], carbon fibre (3.9×10^4 nN m)[33] and thin-film electronic ($0.16–1.3 \times 10^4$ nN m)[12,13,35] probes (Supplementary Section 5.2.2). The flexibility of the injected electronics is closer to the flexibility of the tissue, which has been demonstrated to minimize mechanical trauma caused by the relative motion between the probe and surrounding tissue[33,35]. In addition, the feature sizes of our injected mesh electronics (5–20 μm) are less than or equal to those of single cells, which can also reduce chronic damage, even when the probe stiffness is much greater than that of the tissue[33].

Finally, we verified the ability of the injected mesh electronics to record brain activity in the HIP of anaesthetized mice (Fig. 4k,i and Supplementary Fig. 13). Representative multichannel recordings using mesh electronics with Pt-metal electrodes (Fig. 4k) yielded well-defined signals in all 16 channels. The modulation amplitude (200–400 μV) and dominant modulation frequency (1–4 Hz) recorded are characteristic of δ-wave local field potentials (LFPs) in anaesthetized mice. Moreover, spatiotemporal mapping of the LFP recordings (Supplementary Fig. 13d) revealed characteristic hippocampal field activity for the rodent brain[36,37]. standard analysis (see Methods)[38,39] of the sharp downward spikes (Fig. 4l) showed a

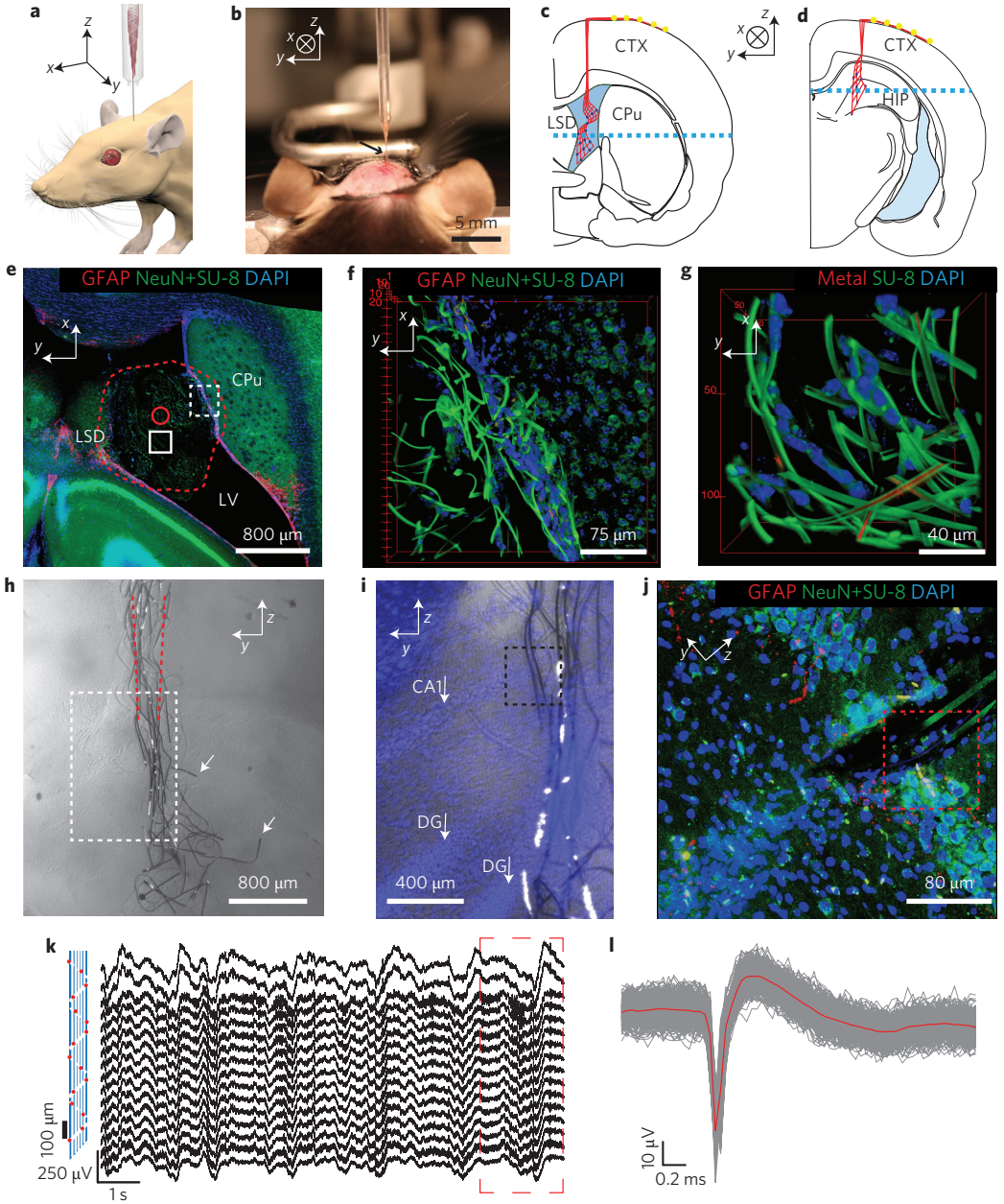

Figure 4 | Syringe-injectable electronics into an *in vivo* biological system. a, Schematic shows *in vivo* stereotaxic injection of mesh electronics into a mouse brain. **b**, Optical image of the stereotaxic injection of mesh electronics into an anaesthetized three-month-old mouse brain. **c**,**d**, Schematics of coronal slices illustrating the two distinct areas of the brain into which mesh electronics were injected: through the cerebral cortex (CTX) and into the lateral ventricle (LV) cavity adjacent to the caudoputamen (CPu) and lateral septal nucleus (LSD) (**c**) and through the CTX into the hippocampus (HIP) (**d**). Red lines highlight and indicate the overall structure of the mesh, and dark blue filled circles indicate recording devices. The blue dashed lines indicate the direction of horizontal slicing for imaging. **e**, Projection of the 3D reconstructed confocal image from a 100-µm-thick, 3.17-mm-long and 3.17-mm-wide volume horizontal slice five weeks post-injection at the position indicated by the blue dashed line in **c**. The red dashed line highlights the boundary of the mesh inside the LV, and the solid red circle indicates the size of the needle used for injection. Red, green and blue colours correspond to GFAP, NeuN/SU-8 and DAPI, respectively, and are denoted at the top of the image panel in this and subsequent images. **f**, 3D reconstructed confocal image from the dashed red box in Supplementary Fig. 8a at the interface between the mesh electronics and subventricular zone (SVZ). **g**, 3D reconstructed confocal image from the dashed red box in Supplementary Fig. 8c at the approximate middle (of the *x*–*y* plane) of the LV in the slice. **h**, Bright-field microscopy image of a coronal slice of the HIP region five weeks post-injection of the mesh electronics. Red dashed lines indicate the boundary of the glass needle. White arrows indicate longitudinal elements that were broken during tissue slicing. **i**, Overlaid bright-field and epi-fluorescence images from the region indicated by the white dashed box in **h**. Blue corresponds to DAPI staining of the cell nuclei, and white arrows indicate CA1 and the dentate gyrus (DG) of the HIP. **j**, Projection of the 3D reconstructed confocal image from a 30-µm thick, 317-µm-long and 317-µm-wide volume from the zoomed-in region highlighted by the black dashed box in **i**. **k**, Acute *in vivo* 16-channel recording using mesh electronics injected into a mouse brain. The devices were Pt-metal electrodes (impedance ~950 kΩ at 1 kHz) with their relative positions marked by red spots in the schematic (left panel), and the signal was filtered with 60 Hz notch during acquisition. The dashed red rectangle indicates the section used for spatiotemporal mapping of multichannel-LFP recordings (Supplementary Fig. 12d). **l**, Superimposed single-unit neural recordings from one channel after 300–6,000 Hz band-pass filtering. The red line represents the mean waveform for the single-unit spikes.

uniform potential waveform with average duration of ~2 ms and peak-to-peak amplitude of ~70 μV characteristic of single-unit action potentials[33]. In the context of long-term chronic recording, our histology results and previous work[12,13,15] demonstrate the biocompatibility and long-term stability of using SU-8 passivated interconnects, and the long-term stability of metal oxide passivated silicon nanowire sensors[15,40]. Hence, we believe these results, together with the 'neurophilic' chronic response, offer substantial promise for implantation and long-term brain activity mapping[41].

Conclusions

In summary, we have introduced a new strategy for delivering electronics to the internal regions of 3D man-made and biological structures that involves the syringe injection of submicrometre-thickness, large-area macroporous mesh electronics. We have shown that mesh electronics with widths more than 30 times the needle ID can be injected and maintain a high yield of active electronic devices. *In situ* imaging and modelling show that optimizing the transverse and longitudinal stiffness enables the mesh to 'roll up' when passing through needle constrictions. We have demonstrated that injected mesh electronics with addressable piezoresistive devices are capable of monitoring internal mechanical strains within bulk structures, and have also shown that mesh electronics injected into the brains of mice exhibit little chronic immunoreactivity, attractive interactions with neurons, and can reliably monitor brain activity. Compared to other delivery methods[9–18], our syringe injection approach allows the delivery of large (with respect to the injection opening) flexible electronics into cavities and existing synthetic materials through small injection sites and relatively rigid shells. In the future, our new approach and results could be extended in several directions, including the incorporation of multifunctional electronic devices[7,13,16,42] and/or wireless interfaces[13,43] to further increase the complexity of the injected electronics. Additionally, recent reports[42,44–46] have demonstrated that novel electrophysiological recordings enabled by nanoelectronic units require an intimate nanoelectronics/cellular interface. In this emerging direction, our syringe-injectable electronics could serve as a unique yet general platform for building direct neuron–nanoelectronics interfaces for *in vivo* studies. Finally, syringe injection brings the opportunity to co-inject mesh electronics with a polymer precursor or cells into host systems for unique engineering and biomedical applications.

Methods

Methods and any associated references are available in the online version of the paper.

Received 14 December 2014; accepted 28 April 2015; published online 8 June 2015

References

1. Kaltenbrunner, M. *et al.* An ultra-lightweight design for imperceptible plastic electronics. *Nature* **499,** 458–463 (2013).
2. Timko, B. P. *et al.* Electrical recording from hearts with flexible nanowire device arrays. *Nano Lett.* **9,** 914–918 (2009).
3. Kim, D. *et al.* Epidermal electronics. *Science* **333,** 838–843 (2011).
4. Wang, C. *et al.* User-interactive electronic skin for instantaneous pressure visualization. *Nature Mater.* **12,** 899–904 (2013).
5. Tee, B. C. K., Wang, C., Allen, R. & Bao, Z. An electrically and mechanically self-healing composite with pressure- and flexion-sensitive properties for electronic skin applications. *Nature Nanotech.* **7,** 825–832 (2012).
6. Takei, K. *et al.* Nanowire active-matrix circuitry for low-voltage macroscale artificial skin. *Nature Mater.* **9,** 821–826 (2010).
7. Mannoor, M. S. *et al.* Graphene-based wireless bacteria detection on tooth enamel. *Nature Commun.* **3,** 763 (2012).
8. Sekitani, T. *et al.* A rubberlike stretchable active matrix using elastic conductors. *Science* **321,** 1468–1472 (2008).
9. Mathieson, K. *et al.* Photovoltaic retinal prosthesis with high pixel density. *Nature Photon.* **6,** 391–397 (2012).
10. Mandel, Y. *et al.* Cortical responses elicited by photovoltaic subretinal prostheses exhibit similarities to visually evoked potentials. *Nature Commun.* **4,** 1980 (2013).
11. Kim, D. *et al.* Materials for multifunctional balloon catheters with capabilities in cardiac electrophysiological mapping and ablation therapy. *Nature Mater.* **10,** 316–323 (2011).
12. Rousche, P. J. *et al.* Flexible polyimide-based intracortical electrode arrays with bioactive capability. *IEEE Trans. Biomed. Eng.* **48,** 361–371 (2001).
13. Kim, T. *et al.* Injectable, cellular-scale optoelectronics with applications for wireless optogenetics. *Science* **340,** 211–216 (2013).
14. Kane, M. J., Breen, P. P., Quondamatteo, F. & Olaighin, G. BION microstimulators: a case study in the engineering of an electronic implantable medical device. *Med. Eng. Phys.* **33,** 7–16 (2011).
15. Tian, B. *et al.* Macroporous nanowire nanoelectronic scaffolds for synthetic tissues. *Nature Mater.* **11,** 986–994 (2012).
16. Liu, J. *et al.* Multifunctional three-dimensional macroporous nanoelectronic networks for smart materials. *Proc. Natl Acad. Sci. USA* **110,** 6694–6699 (2013).
17. Kim, D. *et al.* Dissolvable films of silk fibroin for ultrathin conformal bio-integrated electronics. *Nature Mater.* **9,** 511–517 (2010).
18. Kim, D. *et al.* Electronic sensor and actuator webs for large-area complex geometry cardiac mapping and therapy. *Proc. Natl Acad. Sci. USA* **109,** 19910–19915 (2012).
19. Yim, M. & Paik, K. The contact resistance and reliability of anisotropically conductive film (ACF). *IEEE Trans. Adv. Packag.* **22,** 166–173 (1999).
20. Stieglitz, T. in *Handbook of Neural Activity Measurement* (eds Brette, R. & Destexhe, A.) 8–43 (Cambridge Univ. Press, 2012).
21. Cogan, S. F. Neural stimulation and recording electrodes. *Annu. Rev. Biomed. Eng.* **10,** 275–309 (2008).
22. Cui, Y., Wei, Q., Park, H. & Lieber, C. M. Nanowire nanosensors for highly sensitive and selective detection of biological and chemical species. *Science* **293,** 1289–1292 (2001).
23. Bilston, L. E. *Neural Tissue Biomechanics* (Springer, 2011).
24. Hillel, A. T. *et al.* Photoactivated composite biomaterial for soft tissue restoration in rodents and in humans. *Sci. Transl. Med.* **3,** 93ra67 (2011).
25. Bible, E. *et al.* Attachment of stem cells to scaffold particles for intra-cerebral transplantation. *Nature Protoc.* **4,** 1440–1453 (2009).
26. Cetin, A., Komai, S., Eliava, M., Seeburg, P. H. & Osten, P. Stereotaxic gene delivery in the rodent brain. *Nature Protoc.* **1,** 3166–3173 (2006).
27. Alvarez-Buylla, A. & Garcia-Verdugo, J. M. Neurogenesis in adult subventricular zone. *J. Neurosci.* **22,** 629–634 (2002).
28. Goldman, S. Stem and progenitor cell-based therapy of the human central nervous system. *Nature Biotechnol.* **23,** 862–871 (2005).
29. van Dommelen, J. A. W., van der Sande, T. P. J., Hrapko, M. & Peters, G. W. M. Mechanical properties of brain tissue by indentation: interregional variation. *J. Mech. Behav. Biomed. Mater.* **3,** 158–166 (2010).
30. Biran, R., Martin, D. C. & Tresco, P. A. Neuronal cell loss accompanies the brain tissue response to chronically implanted silicon microelectrode arrays. *Exp. Neurol.* **195,** 115–126 (2005).
31. Mercanzini, A. *et al.* Demonstration of cortical recording using novel flexible polymer neural probes. *Sens. Actuat. A* **143,** 90–96 (2008).
32. Symour, J. P. & Kipke, D. R. Neural probe design for reduced tissue encapsulation in CNS. *Biomaterials* **28,** 3594–3607 (2007).
33. Yoshida Kozai, T. D. *et al.* Ultrasmall implantable composite microelectrodes with bioactive surfaces for chronic neural interfaces. *Nature Mater.* **11,** 1065–1073 (2012).
34. Lee, H., Bellamkonda, R. V., Sun, W. & Levenston, M. E. Biomechanical analysis of silicon microelectrode-induced strain in the brain. *J. Neural Eng.* **2,** 81–89 (2005).
35. Navarro, X. *et al.* A critical review of interfaces with the peripheral nervous system for the control of neuroprostheses and hybrid bionic systems. *J. Peripher. Nerv. Syst.* **10,** 229–258 (2005).
36. Buzsaki, G. *et al.* Hippocampal network patterns of activity in the mouse. *Neuroscience* **116,** 201–211 (2003).
37. Agarwal, G. *et al.* Spatially distributed local fields in the hippocampus encode rat position. *Science* **344,** 626–630 (2014).
38. Morris, G., Arkadir, D., Nevet, A., Vaadia, E. & Bergman, H. Coincident but distinct messages of midbrain dopamine and striatal tonically active neurons. *Neuron* **43,** 133–143 (2004).
39. Zhang, J. *et al.* Integrated device for optical stimulation and spatiotemporal electrical recording of neural activity in light-sensitized brain tissue. *J. Neural Eng.* **6,** 055007 (2009).
40. Zhou, W. *et al.* Long term stability of nanowire nanoelectronics in physiological environments. *Nano Lett.* **14,** 1614–1619 (2014).
41. Alivisatos, P. A. *et al.* The brain activity map. *Science* **339,** 1284–1285 (2013).
42. Almquist, B. D. & Melosh, N. A. Fusion of biomimetic stealth probes into lipid bilayer cores. *Proc. Natl Acad. Sci. USA* **107,** 5815–5820 (2010).

43. Wise, K. D., Anderson, D. J., Hetke, J. F., Kipke, D. R. & Najafi, K. Wireless implantable microsystems: high-density electronic interfaces to the nervous system. *Proc. IEEE* **92,** 76–97 (2004).
44. Tian, B. *et al.* Three-dimensional, flexible nanoscale field-effect transistors as localized bioprobes. *Science* **329,** 831–834 (2010).
45. Duan, X. *et al.* Intracellular recordings of action potentials by an extracellular nanoscale field-effect transistor. *Nature Nanotech.* **7,** 174–179 (2012).
46. Spira, M. *et al.* Multi-electrode array technologies for neuroscience and cardiology. *Nature Nanotech.* **8,** 83–94 (2013).

Acknowledgements

The authors thank J.L. Huang for *in vivo* scaffold fabrication. C.M.L. acknowledges support from a National Institutes of Health Director's Pioneer Award, the Air Force Office of Scientific Research and the Star Family Fund.

Author contributions

J.L., T.F., Z.C. and C.M.L. designed the experiments. J.L., T.F., Z.C., G.H., T.Z., M.D. and Z.J. performed the experiments. L.J. and Z.S. performed FEM analysis. J.L., T.F., Z.C. and C.M.L. analysed the data and wrote the manuscript. J.L., T.F., Z.C., G.H., T.Z., L.J., M.D., Z.J., P.K., C.X., Z.S., Y.F. and C.M.L. discussed manuscript.

Additional information

Supplementary information is available in the online version of the paper. Reprints and permissions information is available online at www.nature.com/reprints. Correspondence and requests for materials should be addressed to Y.F. and C.M.L.

Competing financial interests

The authors declare no competing financial interests.

Methods

Free-standing injectable mesh electronics were fabricated on a nickel relief layer as reported previously[15,16]. Following release from the substrate, the mesh electronics were modified by poly-D-lysine (M_W = 70,000–150,000, Sigma-Aldrich) and then loaded into a syringe fitted with either a metal needle or a glass needle pulled by a commercially available pipette puller (Model P-97, Sutter Instrument). A microinjector (NPIPDES, ALA Scientific Instruments) and manually controlled syringes (Pressure Control Glass Syringes) were used to inject the electronics. Needles with an ID of 400 μm were used to investigate mesh electronics injection as a function of the fluid flow rate. Smooth mesh electronics injection can be established for flows from 20 to 150 ml h^{-1} as long as the needle retraction speed matches the speed of the injected fluid. The lower limit for smooth injection, 20 ml h^{-1}, is believed to be restricted by the smallest fluid drag force relative to the friction force between the rolled-up mesh electronics and the inner needle surfaces. The maximum flow (150 ml h^{-1}) was limited by the needle retraction speed of the set-up. To characterize the structures of different mesh electronics within glass needle-like constrictions to understand the design parameters for successful injection, a pulled glass tube with controlled ID central constriction was positioned under a microscope objective for bright-field and confocal fluorescence imaging, and the mesh electronics were partially injected through the constriction. Confocal microscopes (Olympus Fluoview FV1000 and Zeiss LSM 780) were used to image the structure of the mesh electronics in the glass channels and immunostained mouse brain slices. ACF (AC-4351Y, Hitachi Chemical) bonding to the mesh electronics I/O was carried out using a home-made or commercial bonding system (Fineplacer Lambda Manual Sub-Micron Flip-Chip Bonder, Finetech) with a flexible cable (FFC/FPC Jumper Cables PREMO-FLEX, Molex).

The PDMS cavity was designed with a step-like internal corrugation (four steps, 0.1 cm drop/step and a projected cavity area of 2×4.8 cm^2). The strain response of silicon nanowire piezoresistive strain sensors was measured by a multi-channel current/voltage preamplifier (Model 1211, DL Instruments), filtered with a 3 kHz low-pass filter (CyberAmp 380, Molecular Devices) and digitized at a 1 kHz sampling rate (AxonDigi1440A, Molecular Devices), with a 100 mV d.c. source bias voltage.

In a typical procedure for *in vivo* brain recording from metal electrodes, a 100–200 μm ID glass needle loaded with mesh electronics, mounted in the stereotaxic apparatus and connected to a microinjector, was positioned to a specific coordinate in the brain of an anaesthetized mouse and the mesh was then injected concomitantly with retraction of the needle so that the electronics was extended in the longitudinal (injection) direction. The flexible cable was connected to a 32-channel Intan RHD 2132 amplifier evaluation system (Intan Technologies) with an Ag/AgCl electrode acting as the reference. A 20 kHz sampling rate and 60 Hz notch were used during acute recording. A 300–6,000 Hz bandpass filter[38] and spike-sorting algorithm[39] were used for single-unit action potential data analysis.